





Article

An Investigation on Reduction of Calcium Added Bauxite Residue Pellets by Hydrogen and Iron Recovery through Physical Separation Methods

Ahmad Hassanzadeh ^{1,*}, Manish K. Kar ², Jafar Safarian ² and Przemyslaw B. Kowalczyk ¹

¹ Department of Geoscience and Petroleum, Faculty of Engineering, Norwegian University of Science and Technology, Andersens veg 15a, 7031 Trondheim, Norway; przemyslaw.kowalczyk@ntnu.no

² Department of Materials Science and Engineering, Norwegian University of Science and Technology, Alfred Getz vei 2, 7491 Trondheim, Norway; manish.k.kar@ntnu.no (M.K.K.); jafar.safarian@ntnu.no (J.S.)

* Correspondence: ahmad.hassanzadeh@ntnu.no; Tel.: +49-176-2066-6711

Abstract: This study investigates the properties of H₂-reduced calcium-added bauxite residue, self-hardened pellets, and the feasibility of iron recovery through electrostatic and magnetic separation methods. The oxide pellets are prepared via a mixing of bauxite residue, calcite, and quicklime. The self-hardened pellets are reduced at 1000 °C with hydrogen gas flow for 120 min. The chemical composition, phase identification, and microstructural observations are executed using X-ray fluorescence (XRF), X-ray diffraction (XRD), and scanning electron microscopy (SEM), respectively. The porosity and strength of the self-hardened pellets are performed by the Mercury intrusion porosimetry and tumbling tests, respectively. The separation of iron is examined through a dry electrostatic technique, and in wet conditions, i.e., via Davis Tube and low-intensity magnetic separation (WLIMS). The effect of the magnetic field (0.1, 0.25, and 0.32 T) is tested on two different particle size fractions (−212 + 106 μm and −106 + 74 μm). It is found that most of the iron oxide in the bauxite residue is converted to metallic iron, which corresponds well with both XRD and SEM results. The Carpc electrostatic tests indicate that this approach is inefficient for the studied type of material because of the intensive association of iron with the rest of the components leading to transferring it to the middling rather than to conductive product. However, both the Davis Tube and WLIMS approve a reasonable improvement in the Fe content from 22% to 37% with acceptable recoveries. The results of the Davis Tube show that there is an optimum magnetic field and particle size for maximization of Fe grade and recovery. Finally, further suggestions are highlighted for the physical beneficiation of studied bauxite residue with the purpose of maximizing iron grade and recovery.

Keywords: H₂-reduced bauxite residue; electrostatic and magnetic separations; iron oxides; pelletizing; decarbonization



Citation: Hassanzadeh, A.; Kar, M.K.; Safarian, J.; Kowalczyk, P.B. An Investigation on Reduction of Calcium Added Bauxite Residue Pellets by Hydrogen and Iron Recovery through Physical Separation Methods. *Metals* **2023**, *13*, 946. <https://doi.org/10.3390/met13050946>

Academic Editor: Ilhwan Park

Received: 18 April 2023

Revised: 10 May 2023

Accepted: 11 May 2023

Published: 13 May 2023



Copyright: © 2023 by the authors. Licensee MDPI, Basel, Switzerland. This article is an open access article distributed under the terms and conditions of the Creative Commons Attribution (CC BY) license (<https://creativecommons.org/licenses/by/4.0/>).

1. Introduction

Since energy demand has increased globally, concerns regarding the depletion of natural resources and an increase in environmental pollution have become more tangible. The current main energy consumption worldwide originates from fossil fuels, which are the main sources of global warming containing ca. 73% of total greenhouse gases [1,2]. Although several green iron and steel production techniques have been addressed in the literature [3,4] current productions are mainly based on carbothermic processes, which generate a considerable amount of CO/CO₂ gases. In 2019, it was estimated that, on average, 1.85 tons of CO₂ was generated per ton of steel produced. In 2020, the total direct emission of CO₂ from the steel sector was around 2.6 billion tons, which was around (7–9%) of total world anthropogenic CO₂ emissions [5]. Thus, the replacement of carbon in iron oxide reduction by hydrogen as a reductant can be a green technology because it is associated with a water vapor outlet in place of emitting CO/CO₂. The direct reduction

of iron oxides with hydrogen has several technical advantages, such as the substitution of expensive metallurgical coke, lowering carbon content in the pig iron, and $\text{H}_2\text{O}/\text{H}_2$ as the product gases compared to CO/CO_2 in the carbon reduction [6].

Several investigations have reported the process of hydrogen reduction of bauxite residue (BR) and bauxite. In this regard, Skibelid et al. [7] study the isothermal hydrogen reduction of BR, calcite (CaCO_3) sintered pellets at high temperatures. They indicate that reduction kinetics is the fastest at 1000 °C than 1100 and 1200 °C, which could be due to porosity loss by sintering and a change in a reduction mechanism to a diffusion-controlled step. Recently, Pilla et al. [8] examine the conversion of hematite (Fe_2O_3) to magnetite (Fe_3O_4) for BR and study the magnetic separation of magnetite and alumina (in the form of sodium aluminate) after water leaching. They find that at 500 °C, the maximum conversion of 96% occurs using 20% NaOH and 5 vol.% hydrogen for 120 min. Following this, Hassanzadeh et al. [9] report that under optimum reduction conditions (5 vol.% H_2 gas at a respective temperature and time of 500 °C and 2 h with 20 wt% NaOH) and optimized process circumstances (particle size: $-106 + 74 \mu\text{m}$, and magnetic intensity of 0.1 T) the Fe content increases from 20% to 41% with the mass recovery of 51%. Hydrogen reduction of a bauxite ore is studied by Lazou et al. [10] for the iron separation prior to the ore smelting. It is indicated that the reduction of hematite to iron begins below 560 °C, and the rate and extent of reduction enhances with increasing temperature. However, the formation of hercynite (FeAl_2O_4) retards the complete reduction above 760 °C. The addition of sufficient Ca to BR avoids the hercynite formation during the reduction step. Following these literature data, it is clear that optimum values of operating parameters (e.g., temperature, time, and leaching properties) using H_2 as a reductant requires further investigation. Additionally, there is not sufficient information regarding the reduction process followed by the separation techniques, which is the matter of the present paper.

Another serious concern is related to waste management: its valorization and environmental issues of tailings that not only lead to water and air pollutions [11] but also occupy massive areas and whose collapse creates human and animal casualties [12]. For instance, in 2010, the Ajka red mud depository located in western Hungary led to disposing of 1 million m^3 alkaline slurry (pH > 11) to the environment, 10 deaths, and over 120 injuries [13]. A similar tragedy took place at the Fundão tailings dam (Brazil), which released 43 million m^3 of iron ore tailings, causing environmental damage and polluting 668 km of watercourses from the Doce River Basin to the Atlantic Ocean [14]. On the other hand, it is certainly beneficial to use secondary resources to extract critical valuable elements embedded in such disposals through mineral processing treatments. In the case of the aluminum (Al) industry, which generates Al from the Bayer process [15] of bauxite ores (i.e., gibbsite ($\text{Al}(\text{OH})_3$), boehmite ($\text{AlO}(\text{OH})$), and diasporite ($\text{AlO}(\text{OH})$)), tailings remain as bauxite residue and contain a polymetallic source of invaluable elements, e.g., iron oxides (as the main component), REEs (rare earth elements), Sc, Ti, Cu, Cr, and silicates [16,17].

Over the last four decades, many research works have focused on recovering Fe from red muds using pyrometallurgical processes [18], hydrometallurgical approaches [19], combined pyrometallurgical and hydrometallurgical techniques [20], Donnan dialysis [21], and direct magnetic separation [22]. Sadangi et al. [23] attempt to recover iron from a red mud dump after a series of processes, i.e., blending (0.5% of bentonite), pelletizing, atmospheric drying (48 h), reducing with coal ($-6 + 3 \text{ mm}$) at an electrical furnace, grinding ($<45 \mu\text{m}$), and wet low-intensity magnetic separation (WLIMS, fixed magnetic field of 0.18 T). Ultimately, the iron content (32%) in the feed is concentrated to 65% of Fe with a recovery of 61%. In another research study, Habibi et al. [24] apply carbothermal reduction, magnetic separation (Davis Tube, 1000 G, %S = 3–4%, water flowrate = 1.42 L/min, and solid flowrate = 40–46 g/min), and leaching for recovering Ti, Al, REEs, and Fe from the red mud (Jajarm Alumina complex, Iran, feed Fe = 19%). The effect of particle size (d_{80} , 35, 100, and 223 μm) are examined under optimum reduction conditions ($T = 1350 \text{ }^\circ\text{C}$, $t = 120 \text{ min}$, coal/red mud = 3 and ash/red mud = 0.2). It is recognized that the Fe recovery is maximized (75%) when the d_{80} is 100 μm , while finer and coarse sizes than that lead to

the recovery of 9% and 40%, respectively. Gotsu et al. [25] convert hematite to magnetite by employing a tube furnace and reduction at 550 °C. The results show 60% of Fe in the final concentrate using dry and wet magnetic separators. Ksiazek et al. [26] also report 43% beneficiation on the Fe content from a CO-H₂-reduced bauxite residue. Following these studies, several works have attempted, under different conditions, to upgrade the Fe content with a reasonable mass recovery; however, they are mainly based on adding carbon as a reductant than hydrogen. Since there is little information available on the magnetic behavior of H₂-reduced bauxite residue, this study investigates this subject for the first time.

It is estimated that the global aluminum consumption will reach from ca. 66 (2022) to ca. 78 million metric tons in 2029, and it is accompanied by approximately double the mass of BR production per mass of Al metal. This has also a direct impact on increasing the CO₂ level, which is predicted to be ca. 700 ppm in 2040 and can be significantly diminished by substituting H₂ as a reductant instead of using carbon in metal production. Therefore, this work explores the physical and chemical properties of bauxite residue reduced by H₂ at various temperatures as well as examines the recoverability of Fe using electrostatic and magnetic separation techniques. To the best of the authors' knowledge, such information is not available in the literature and surely will be helpful for the development of employing hydrogen and producing green Fe from the bauxite residue in the future.

2. Materials and Methods

2.1. Pelletizing and Hydrogen Reduction

Bauxite residue (BR, filter cake), calcite (CaCO₃), and quick lime (CaO) were supplied from the Mytilineos Business Unit S.A., Greece (previously known as aluminum of Greece), VUGLUKLI S.A. Greece, and NorFrakalk, respectively. The sampling campaign was executed through several days during July (2021) and 1 ton of the tailing was gathered, paying close attention to the representatives of the samples, and shipped to Norway. These materials were dried at 80 °C overnight and later deagglomerated in the ball mill to a size below 500 µm. Afterward, these materials were mixed in the appropriate ratio to maintain the CaO/Al₂O₃ = 1 in the mixture despite chemical composition with the purpose of forming a calcium aluminate leachable phase. Calcium was used in the form of CaO and CaCO₃ with proportions of 10% CaO and 90% CaCO₃. The mixed bauxite residue, limestone, and quick lime were utilized for pelletization in a drum pelletizer via 10 wt.% addition of water. The homogenized mixture was used for the pelletization process in a lab-scale drum pelletizer with a rotation speed of 300 rpm for 15 min. These green pellets were dried in an oven at 80 °C overnight.

The hydrogen reduction was carried out on the dry pellets using a bench-scale vertical tube furnace whose schematic overview is shown in Figure 1. Initially, the cylindrical stainless-steel crucible was loaded with pellets and vertically inserted from the top of the furnace. The gas inlet valve was connected from the bottom through the crucible and off-gases came out from the top and went directly to the hood. Two thermocouples were applied; one was inserted into the middle of the pellets bed and another one on the furnace wall. The heating rate and desired temperatures were controlled based on both thermocouple temperature readings. The heating rate was initially around 20 °C/min up to the temperature of 600 °C, and then 10 °C/min to reach the target temperature of 1000 ± 20 °C. Heating and cooling processes were performed in the presence of argon (purity 99.99 vol%) with a flow of 1 NL/min. Before reduction, the crucible was flashed with argon to remove potential gas contamination present inside. The reduction was carried out in the presence of pure hydrogen (purity 99.999 vol%) with a flow rate of 4 NL/min for 120 min. The stoichiometric amount of H₂ was purged during reduction, which was more than the stoichiometric value for reducing the amount of oxygen present in the iron complexes. After the reduction, the reduced pellets were cooled down in the presence of argon to prevent the reoxidation of metallic iron.

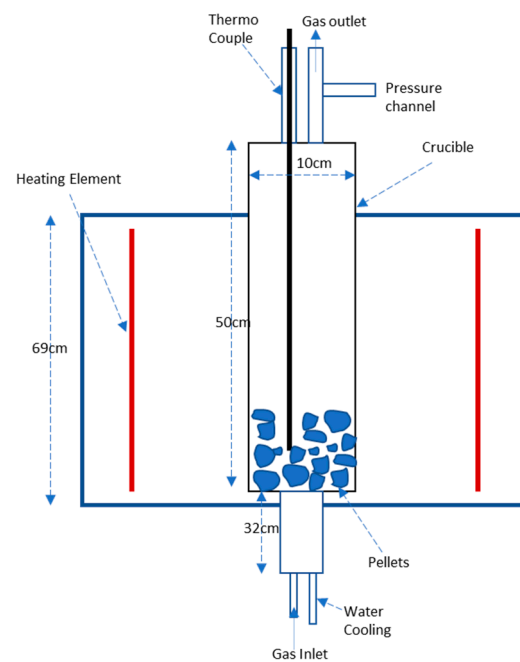


Figure 1. A schematic view of the reduction furnace including its different components.

To check the amount of weight loss and phase formation during the heating cycle, the dry pellets were sintered in a muffle furnace with a shocking time of 60 min at 1000 °C. The color of dry pellets was changed from reddish to brownish in sintering, then to dark grey/black after reduction, shown in Figure 2.

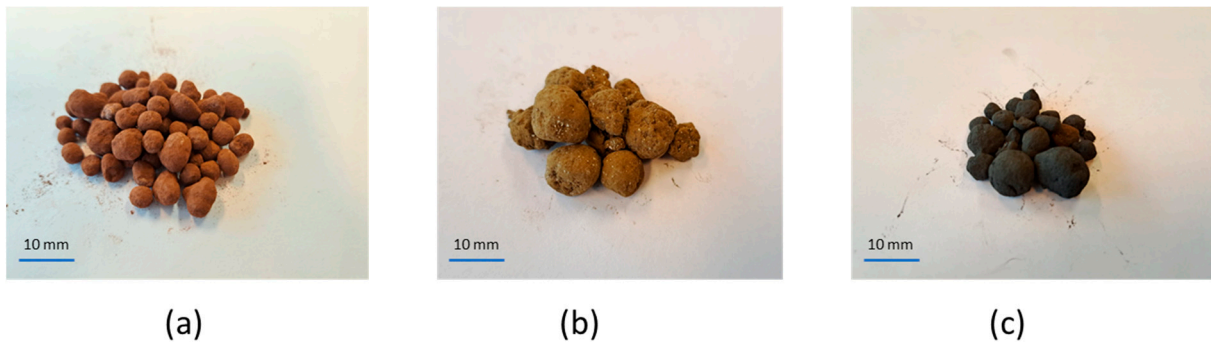


Figure 2. An illustration of (a) dried, (b) sintered, and (c) hydrogen-reduced pellets.

2.2. Sample Preparation and Experimental Methodology

The pellets of H₂-reduced bauxite residue were subjected to the pretreatment procedure before conducting the physical separation experiments (Figure 3). First, the pellets were ground step-wised using a laboratory jaw crusher (Retsch®, Germany). As a normal procedure, the jaw crusher was cleaned a few times with quartz and then ethanol to prevent any external contamination. The ground samples were sieved in a dry environment using a shaker device (RX-29H&B, ROT-AP®, W.S. Tyler, USA) and screens (Tyler standards, Retsch®, Germany) applying 50 g per run, which each lasted 15 min. The samples, after being ground and reaching desirable size fractions, were subjected to three different equipment for separation purposes. Two wet magnetic separators (i.e., Davis Tube and WLIMS (low-intensity magnetic separation) and one dry electrostatic machine (Carpc electrostatic) were applied. Representative samples of the products of each electrostatic experiment (i.e., conductive, non-conductive, and middling) were directly analyzed through an X-ray fluorescence analysis (XRF). The products from magnetic separation tests (i.e., non-magnetic and magnetic) were first filtered using a filter press (MACSLAtB, Eriez, F-Press model,

USA), dried (overnight at 60 °C), and then analyzed by the portable-XRF spectroscopy (pXRF, Thermo Fisher Scientific, UK) which is a semi-quantitative analysis method. Three different points were randomly measured and for each point, three measurements were adjusted using the equipment. Finally, the average values were reported as the final elemental contents. The non-magnetic and magnetic products from the Davis Tube tests at 0.25 T were also analyzed by the XRD method which is described in detail in Section 2.3.



Figure 3. A schematic overview of sample preparation and physical separations.

2.2.1. Electrostatic Separation

Initially, primary experiments were performed on $>1397 \mu\text{m}$ (14 mesh), $-1397 + 500 \mu\text{m}$, and $<500 \mu\text{m}$ (35 mesh) size fractions (Table A1, Appendix A). Since electrostatic results for those coarse particle ranges showed a negligible improvement in Fe enrichment, the specimens were ground further to reach a suitable liberation degree for elemental iron. On the other hand, as known, the finer the particles, the lower the effective impact of electrostatic fields. Having this in mind, fraction sizes of $-212 + 106 \mu\text{m}$, $-106 + 74 \mu\text{m}$, and $<74 \mu\text{m}$ were considered and studied in detail. All three fractions were subjected to a Carpc electrostatic separator (Research and Engineering Inc., Florida, FL, USA) under identical operating conditions of feeder rate: 20–40 g, drum rotation speed: 20–30 rpm, electrode 1:30 V, and electrode 2:30 V. These optimum values were acquired based on a trial and error approach and preliminary test works. Figure 4 exhibits a schematic view of the equipment and its components. Detailed information regarding the separation mechanism can be found elsewhere [27–29]. It is worth noting that the experiments were conducted once due to the lack of accessibility to the source material and thus the reproducibility of tests should be considered for further analyses.

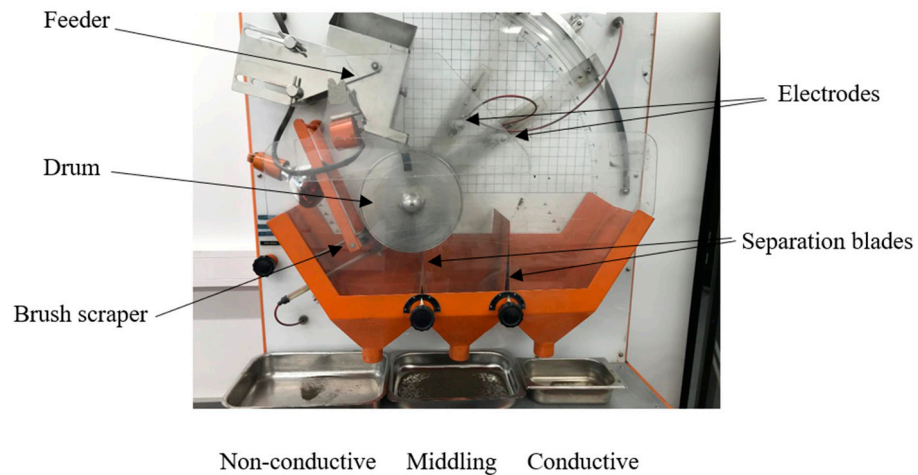


Figure 4. A schematic graph of the Carpc electrostatic device and its different units.

2.2.2. Wet Magnetic Separations

Since the sample consists of only ferromagnetic and paramagnetic entities, low and intermediate magnetic fields were applied. For this reason, two wet magnetic separators, including a Davis Tube (0.02–0.6 T, Dings Magnetic Separator Co., USA) and a low-intensity magnetic separator (SALA, Slot, 0.035 T) were applied. The magnetic fields for each device were measured experimentally using a Gaussmeter but with different probes (axial and transverse) depending on the position of the coils.

The Davis Tube was operated in three magnetic fields i.e., 0.1, 0.25, and 0.32 T, for two different feed fraction sizes of $-212 + 106 \mu\text{m}$ and $-106 + 74 \mu\text{m}$. For each test, 20 g of representative sample was used, keeping the operation time almost constant. First, the strike was regulated to have 60 strokes/min and the water flow rate was stabilized at 1 L/min. The prepared sample was added, and the non-magnetic sample was gathered from the bottom of the tube, while the magnetic fraction (concentrate) was obtained by disconnecting the magnetic field at the end of the experiment. The magnetic and non-magnetic products were filtered, dried, weighed, and analyzed using the pXRF method. The recovery was calculated using the well-known equation as $R = (C \times c) / (F \times f) \times 100$ where the $R(\%)$ is the recovery, $C(\text{g})$ and $F(\text{g})$ are the weight of magnetic and non-magnetic products and $c(\%)$ and $f(\%)$ denotes the grade of Fe in the magnetic product and in the feed sample, respectively. The experimental error propagations were calculated based on two repetitions performed for each test at a 95% confidence level.

For the wet low-intensity magnetic separation (WLMS) experiments, 40 g of sample was used per experiment. After conducting the experimental test, both magnetic and non-magnetic samples were filtered using the filter press and dried overnight. The wet low-intensity magnetic separation tests with a fixed magnetic field of 0.035 T were tested on two fraction sizes of $<500 \mu\text{m}$ and $-106 + 74 \mu\text{m}$. The prepared samples were well-mixed using a pump before feeding to the separator. The level of water within the cell was stabilized by regulating feed water, and wash water was used for cleaning the drum and removing the magnetic product. After reaching a steady state condition, the slurry was fed to the cell gathering non-magnetic and magnetic products in separate containers. For these tests, the experiments were conducted once regarding the accessibility to a limited amount of material, and the reproducibility of tests can be considered for further analyses.

2.3. Characterization of Materials

The phase analysis of the feed and separation products was executed by the X-Ray diffraction method (XRD) using Bruker (D8 A25 DaVinciTM, Karlsruhe, Germany) with the $\text{CuK}\alpha$ (wavelength of 1.54 Å) radiation in 2θ range of $10\text{--}80^\circ$ with step size 0.03° . The compositional analysis of these materials was characterized by the X-Ray fluorescence (XRF) using a PANalytical Zetium 4 kW X-ray spectrometer. The sample for XRF was

prepared by a flux fusion method. The fused bead was prepared by mixing flux with powdered sample and heated to around 1100 °C in platinum crucible. The loss on ignition (LOI) of the sample was calculated by heating the sample to 1000 °C for one hour. The microstructural analysis of the treated materials was performed by a scanning electron microscope (SEM) supplied by Zeiss ultra 55LE, Carl Zeiss. Jena, Germany. The elemental distribution was assessed using elemental mapping via energy dispersive spectroscopy (EDS), Bruker AXS, microanalysis GmbH, Berlin, Germany.

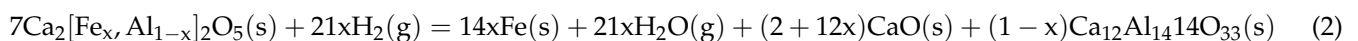
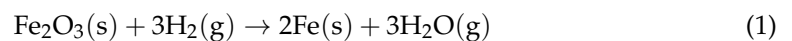
The porosity of green and reduced pellets was measured using an intrusion mercury porosimeter (Autopore IV 9500, Micromeritics, Germany). To measure cold compact compression strength, a compact hydraulic press was used. Measurements were carried out for 5 random pellets and the average values were considered for calculating the breaking load. Tumble and abrasion indices were calculated as per the standard ISO 3271, 3rd edition. For the measurement of tumble and abrasion, the pellet size was used above 7 mm and the dimension of the tumbler was rescaled to a smaller size based on the standard dimension. The dimension of the tumbler was 200 mm inner diameter, 12 mm in length, and four lifters with a height of 6 mm. The abrasion index was calculated based on the weight fraction of fines below 500 µm divided by the total weight of pellets. The tumble index was calculated as the weight fraction above 6.3 mm pellets divided by the total weight. The particle size of the raw material was measured by a laser particle size analyzer (LS COULTER 230, USA). The d_{50} values of bauxite residue, calcite, and lime are 2.2 µm, 1.7 µm, and 1.4 µm, respectively.

3. Results and Discussions

3.1. Mass Changes during Sintering and Reduction

During the heating and reduction cycle, there is a weight loss of around 34.5% of the total weight. It might be due to physisorption and chemisorption water removal at 100 °C, goethite FeO(OH) decomposition at 250 to 300 °C, and the major weight losses were due to the calcite (CaCO₃) and gibbsite (Al(OH)₃) decomposition at 750 to 850 °C [30]. These are the major weight reduction that occur during a heating cycle previously reported by Kar et al. [30]. The weight reduction during a hydrogen reduction cycle is around 9.4%, which is close to the theoretical amount of oxygen present (9.8%) in the iron complexes.

As shown in the XRD patterns of the sintered pellets, iron is present in the form of hematite (Fe₂O₃), and brownmillerite (Ca₂ [Fe_x, Al_(1-x)]₂O₅) (Figure 5), however, in reduced pellets, it is formed as metallic iron. Semi-quantification of the XRD results is executed but the outcomes are not found to be sufficiently accurate, especially for the reduced-bauxite residue sample because all phases are not in the crystal forms and cannot be accurately detected. For this reason, the results are shown in the form of XRD patterns rather than the semi-quantified form. The reduction equations of hematite and brownmillerite are as follows [30]:



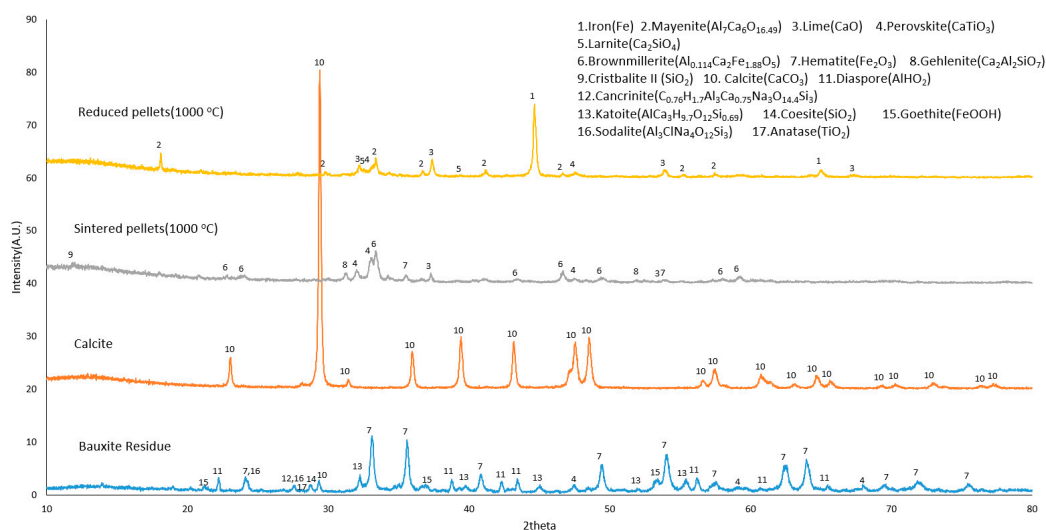
As shown in Equation (1), hematite was directly converted to metallic iron by hydrogen reduction, releasing water vapor as a byproduct. However, the reduction of brownmillerite with hydrogen (Equation (2)) generates mayenite (Ca₁₂Al₁₄O₃₃), CaO, metallic iron, and water vapor. The fraction reduction of the iron oxide was calculated based on Equation (3).

$$\text{Fraction Reduced}(\%X) = \frac{\text{Actual weight loss}(\Delta W_{\text{red}})}{\text{Mass of oxygen present in Fe}_2\text{O}_3 \text{ in initial weight}(W_{\text{in}})} \quad (3)$$

The weight losses in the heating and reduction cycles are presented in Table 1.

Table 1. Weight loss during heating cycle and reduction.

Stage Description	Weight (g)
Dry pellets	50
During heating cycle	16.5
Theoretical mass of O in iron oxide	4.7
During reduction	4.6
Fraction reduction (X)	96.8%

**Figure 5.** XRD patterns of bauxite residue, calcite, sintered pellets, and reduced pellets (0, 20, 40, and 60 are the reference intensities for bauxite residue, calcite, sintered pellets (1000 °C) and reduced pellets (1000 °C) respectively).

3.2. Properties of Products

3.2.1. Chemical Analysis Results

Table 2 presents the XRF analysis results of the most stable oxides of those detected elements. The relative amount of wt.% of the oxide phases are increased in the reduced pellets compared with the dry pellets, which is due to the loss of ignition during heating and mass loss during reduction. The LOI of the limestone is 42.6 wt.% as a result of CO₂ removal during high-temperature ignition. As can be seen, the Fe content measured using the XRF analysis is 21.69%, which is in-line with the result given by the pXRF (22%) for the feed sample. It is worth noting that the relatively lower values for Al₂O₃ and TiO₂ in reduced pellets are mainly related to adding limestone, which indeed diminishes the amounts of those components compared with the bauxite residue. In addition to this, the iron components in bauxite residue, limestone, quick lime, and dry pellets are all in the form of iron oxide (Fe₂O₃) obtained through the XRD results (Figure 5) and the quantitative values in oxide form are provided by the XRF results. However, after the reduction process and for the reduced pellets, the iron oxide is fully converted to the metallic iron. For this reason, only the Fe amount is given in Table 2 and for the rest of materials, the Fe₂O₃ is presented.

Table 2. XRF analysis of bauxite residue (BR), limestone, quicklime, dry pellets, and reduced pellets (wt.%).

Component	Bauxite Residue	Limestone	Quick Lime	Dry Pellets	Reduced Pellets
Al ₂ O ₃	22	0.9	0.24	13.18	20.14
CaO	8.8	52.7	96.7	27.41	39.85
Fe ₂ O ₃	40.71	0.15	0.08	25.03	-
Fe	-	-	-	-	21.69
K ₂ O	0.09	0.12	BDL **	0.05	0.04
MnO	0.08	BDL	BDL	BDL	0.03
MgO	0.23	0.95	0.64	0.42	0.68
Na ₂ O	3.1	BDL	BDL	1.27	1.46
P ₂ O ₅	0.11	0.01	0.02	0.05	0.10
SO ₃	0.95	0.06	BDL	0.45	1.12
SiO ₂	7.1	2.07	0.46	4.24	7.68
TiO ₂	5	0.03	0.02	3.10	4.86
Cr ₂ O ₃	BDL	BDL	BDL	0.17	0.26
NiO	BDL	BDL	BDL	0.08	0.07
L.O.I. *	11.83	43.01	1.84	24.55	2.13

* L.O.I. represents the loss of ignition. ** BDL means below detection limit.

3.2.2. Phase Analysis

Figure 5 shows the XRD spectra of bauxite residue, calcite, sintered dry pellets (1000 °C) and reduced pellets. Iron is present in BR in the forms of hematite and goethite but hematite is the major phase. Aluminum is present in the form of diaspore (AlO(OH)), sodalite (Al₃ClNa₄O₁₂Si₃), and cancrinite (C_{0.76}H_{1.7}Al₃Ca_{0.75}Na₃O_{14.4}Si₃), while titanium is in form of rutile (TiO₂) and perovskite (CaTiO₃). Limestone is a pure compound, which is mostly composed of CaCO₃, and a little amount of MgO and SiO₂ as shown in Table 2. It is found that iron is present in the sintered pellets in the forms of brownmillerite (A_{10.114}Ca₂Fe_{1.88}O₅) and hematite, which indicates that not all iron is converted to brownmillerite during the heating to reduction temperature (1000 °C). In brownmillerite alone with iron, some fraction of aluminum is present, which is due to high temperature diffusion and reactions. The sintered sample also contains gehlenite (Ca₂Al₂SiO₇), perovskite and cristobalite (SiO₂) as major phases. There is a significant difference in phases between sintered and reduced pellets. During hydrogen reduction, both brownmillerite and hematite are converted to the metallic iron. In a reduced sample, most of the alumina is converted to mayenite (Ca₁₂Al₁₄O₃₃), which is an alkali leachable phase. Aside from that, the reduced pellets also contain lime (CaO), perovskite and larnite (Ca₂SiO₄). It is worth mentioning that hydrogen reduction of BR and calcium-sintered pellets have been studied by Skibelid et al. [7]. However, this work focuses on the hydrogen reduction of self-hardened pellets. The phase formation, thermodynamics, and reaction mechanism are different in both sintered and self-hardened pellets during hydrogen reduction.

3.2.3. Microstructural Analysis

The microstructural image and EDS elemental analysis of the self-hardened reduced pellets are shown in Figure 6a–c, respectively. The microstructures of reduced pellets are mainly composed of iron, perovskite, mayenite, and calcium oxide, which is well correlated with the XRD results. However, the brighter phase is metallic iron, and the darker illustrated grey phase is mayenite. As shown in Figure 6a, the metallic iron particles accumulate in some areas. The EDS elemental mapping indicates that the selected elements are broadly distributed, as shown in Figure 6c. These results are in line with the outcomes reported elsewhere [30]. The titanium containing area overlaps with calcium and oxygen, which is in the CaTiO₃ phase, and this is also validated with EDS point analysis. Oxygen is present throughout every phase except iron, which is expected. Iron clustering in some area

might be due to diffusion of reduced iron at high temperatures. The iron particle size of the reduced sample varies from 1 to 10 μm , with an average of 5–6 μm , as seen in Figure 6b.

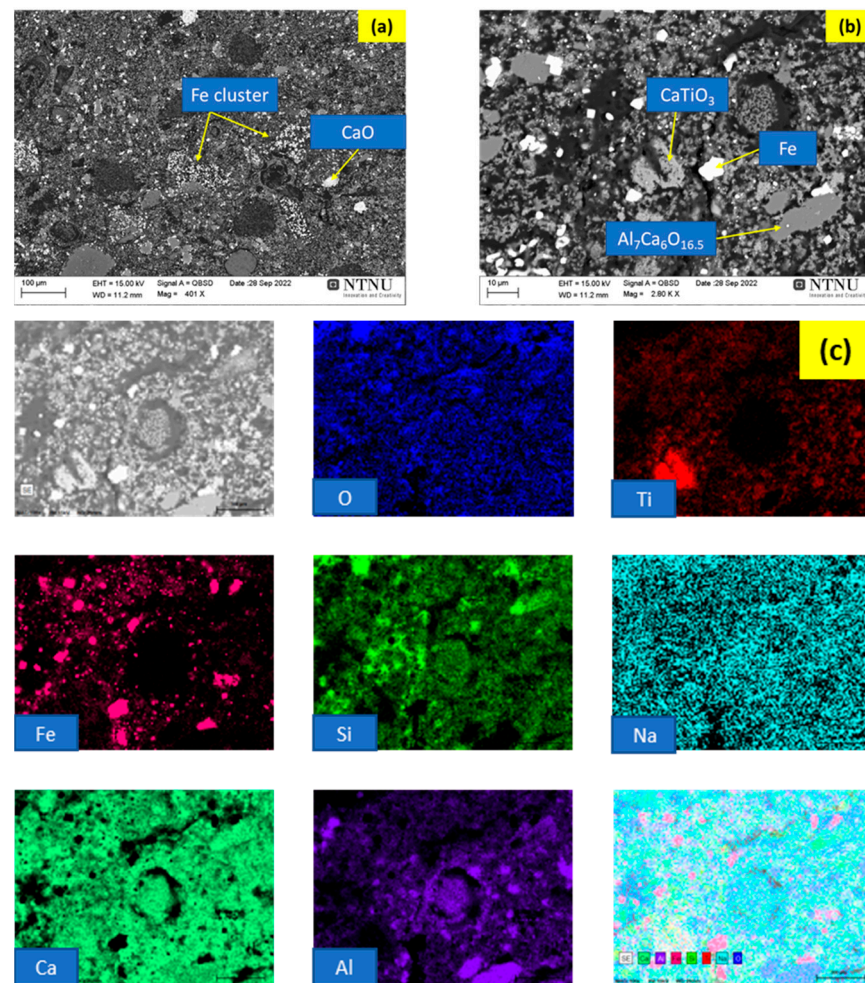


Figure 6. SEM image analysis (a,b) and EDS elemental mapping (c) of reduced pellets.

3.2.4. Physical Properties of Products

The cold compression strength of the pellets (10% CaO/90% CaCO₃) is measured at 0.023 kN as compared with 0.01 kN of 100% CaCO₃ pellets. The CaO-added pellets have more strength as compared with 100% CaCO₃-added pellets, as CaO has cementing properties. During palletization, CaO reacts with H₂O to Ca(OH)₂, which reacts further with atmospheric CO₂ from CaCO₃. The standard free energy (ΔG^0) of the formation of Ca(OH)₂ and CaCO₃ at 1 atm and 0.06 atm is also negative, which signifies the reactions are feasible at room temperature [30]. The tumble and abrasive indices of the CaO-added BR pellets are calculated by mini tumble [31] as 51.3% and 40.7%, respectively. The porosity of pellets was measured by a mercury intrusion porosimeter and is around 45 and 56% for dry and reduced pellets, respectively. The porosity of reduced pellets is mostly due to the CO₂ released during heating. One can notice that the porosity formed during reduction by oxygen removal may not be included in the mercury porosity measurement as mercury had a higher molecular size than oxygen.

3.3. Electrostatic Separation

This beneficiation method fundamentally applies the differences between inherent electrical properties of materials in the feed to separate them by utilizing a high electric voltage [32,33]. According to the electrical conductivity of minerals and the studied sample's characteristics (Figures 5 and 6), they can be categorized into three main groups

i.e., non-conductive (e.g., quartz, calcite, and mayenite), semi-conductive (middling), and conductive (e.g., elemental iron, perovskite, and rutile).

As can be seen from Table 3, the middling contains the main recovery of the product for all size fractions meaning most of the feed is transferred to the middling product during the process. Also, it can be noticed that the recovery of non-conductive parts increases by reducing the particle size. However, the Fe content does not show any substantial change for different size fractions. One plausible reason for this can be the nature of the separation process and material characteristics. In other words, electrostatic separation can only be successful if the individual grains consist only of one component [34]; however, as shown in Figures 5 and 6, the studied material is composed of several intergrowth phases tightly associated with each other. Therefore, a relatively high liberation degree of target particles, in this regard, metallic iron particles, is required to acquire a potentially reasonable separation efficiency. In addition to that, this electrostatic separation technique contains two steps i.e., (i) the charging of particles and (ii) separation. The first step is a particle-surface-based method because electrical conduction mainly takes place on the atomic surface layers [29]. Since the metallic iron is evenly distributed throughout the materials matrix and poly-association of different components with Fe-bearing phases (Figure 6a,b), the Fe content cannot be potentially concentrated in the conductive part. This can be well observed through Figure 6a,b, where the iron components are intensively associated with other phases in the feed material.

Table 3. Results of electro-statistic experiments on three different size fractions.

Fraction Size (μm)		$-500 + 212 \mu\text{m}$	$-212 + 106 \mu\text{m}$	$<74 \mu\text{m}$
Non-conductive	Fe (%)	NA *	24	22
	Recovery (%)	NA	16	32
Middling	Fe (%)	24	23	25
	Recovery (%)	98	82	76
Conductive	Fe (%)	20	18	NA
	Recovery (%)	0.3	5	NA

* NA means not available because of a negligible amount of mass.

3.4. Magnetic Separation

3.4.1. Wet High-Intensity Magnetic Separation

The Davis Tube was operated under its standard condition to investigate the impact of the magnetic field and the particle size on the separation efficiency of studied samples. Figure 7 displays the impact of the magnetic field at three levels i.e., 0.1, 0.25, and 0.32 T on the Fe separation for the fraction size of $-106 + 74 \mu\text{m}$. As can be observed, the lowest magnetic field of 0.1 T induces the maximum Fe content in the magnetic product (35%) but leads to the minimum recovery of 40%. By increasing the field from 0.1 T to 0.25 T, the recovery enhances to 77% but the iron magnitude in the magnetic product diminishes to 27%. Since the metallic iron is heterogeneously disseminated into the material's context as previously shown in Figure 6, applying a 0.25 T magnetic field can increase the amount of iron in the concentrate (i.e., magnetic product) but in an unselective way. A further increase in the magnetic field to 0.32 T leads to an increase in the recovery and enhancement in the iron content, meaning this intensity can be considered as an optimum field of magnetic to reach a favorable separation. To increase the iron grade, the product needs cleaning stages to be purified. In this regard, Pilla et al. [8] present optimum conditions for the hydrogen reduction process and report an improvement of magnetic separation, but no information is addressed regarding the equipment, magnetic intensity, particle size, and other operating parameters.

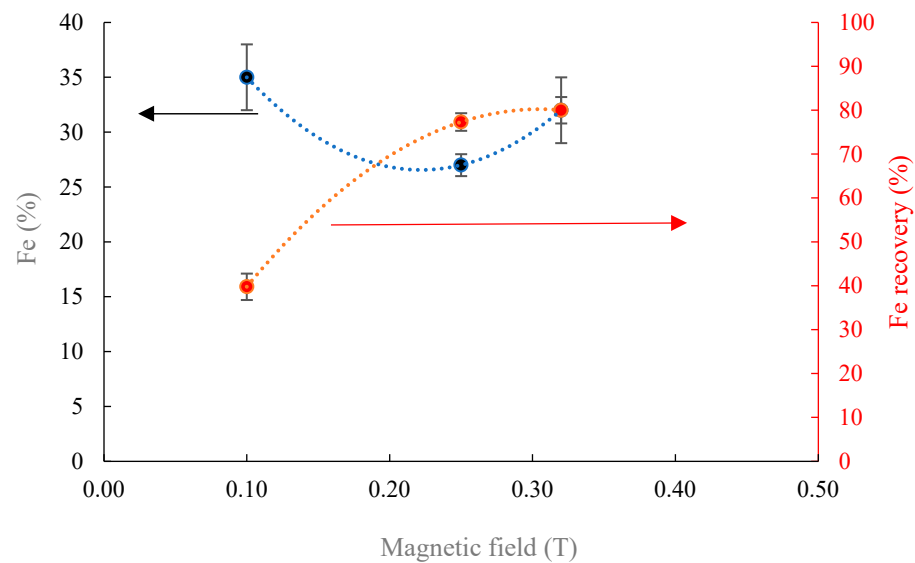


Figure 7. The role of magnetic field on the separation of particles with the size of $-106 + 74 \mu\text{m}$.

Figure 8 exhibits the XRD patterns of non-magnetic and magnetic samples with the particle size $-106 + 74 \mu\text{m}$ obtained through the Davis Tube test at the magnetic field of 0.32 T as presented in Figure 7. There are overall six phases detected in both samples with different intensities i.e., metallic iron (Fe), calcite (CaCO_3), larnite ($\text{Ca}_2\text{O}_4\text{Si}$), perovskite (CaTiO_3), (Fe_2TiO_4), and brownmillerite ($\text{Ca}_2\text{Fe}_2\text{O}_5$). The intensities of the Fe peaks for magnetic products are all higher than non-magnetic ones. The same trend can be recognized for calcite comparing the non-magnetic and magnetic products. Following this, Pilla et al. [35] find the optimum temperature of 600°C to fully convert hematite to magnetite through hydrogen reduction with the purpose of recovering Al and Fe. The maximum Fe recovery is reported as 76.5% using 5 vol% $\text{H}_2 + 95 \text{ vol}\% \text{N}_2$ gas composition at 500°C through water leaching and a wet batch magnetic separation process (liquid to solid ratio of 10, magnetic field of 0.2 T). Since the focus of that study is on reduction and the role of temperature, further information on the non-magnetic and magnetic products is not provided.

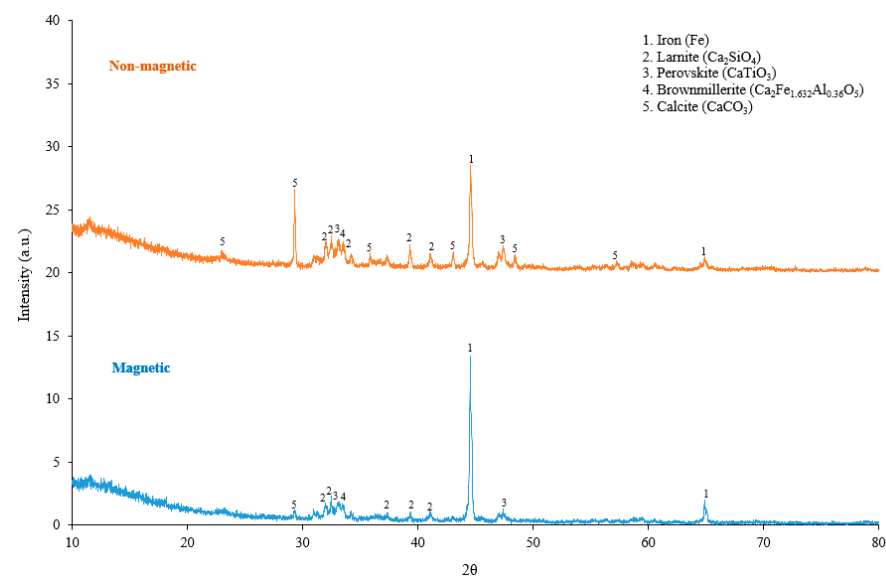


Figure 8. XRD patterns of non-magnetic and magnetic products of the Davis Test at 0.25 T (0 and 20 are reference points for magnetic and non-magnetic products, respectively).

Figure 9 shows the impact of the magnetic field on the coarser size fraction (i.e., $-212 + 106 \mu\text{m}$) under identical operating circumstances. One can see that increasing the magnetic intensity from 0.1 T to 0.2 T slightly improves the Fe recovery from 83% to 90% and the Fe grade from 26% to 30%. Considering both size fractions (Figures 7 and 8), one can conclude that, at the 0.1 T magnetic gradient, coarsening particle size from $-106 + 74 \mu\text{m}$ to $-212 + 106 \mu\text{m}$ leads to the attenuation of the Fe grade from 35% to 25%, and an increase in iron recovery from 40% to 83%. Through this, it is indicated that there is a requirement for examining high magnetic fields followed by low to medium fields. In addition to this, since these tests were performed in batch conditions, applying a continuous treatment mode might be more effective and lead to increase in both grade and recovery simultaneously. In a similar study, Habibi et al. [24] assess the impact of feed particle size (i.e., d_{80} of 35, 100, and 223 μm) on Fe recoverability of a reduced Al residue under optimum conditions of temperature 1350 °C, time 120 min, coal/red mud = 3 and ash/red mud = 0.2 using the Davis Tube operated at 0.1 T. They find that the Fe recovery is maximized (75%) at d_{80} of 100 μm , while for finer and coarse fractions it is 9% and 40%, respectively. However, no information is reported concerning the Fe grades. A relatively similar reduction process is applied on the Greek BR (Fe_2O_3 :45 wt%) using NaOH as an additive and roasting with pure hydrogen for 2 h at 500, 550 and 600 °C. Applying thermal treatment followed by milling and water leaching results in producing Fe-rich residue with an approximative Fe content of 38 wt% [36].

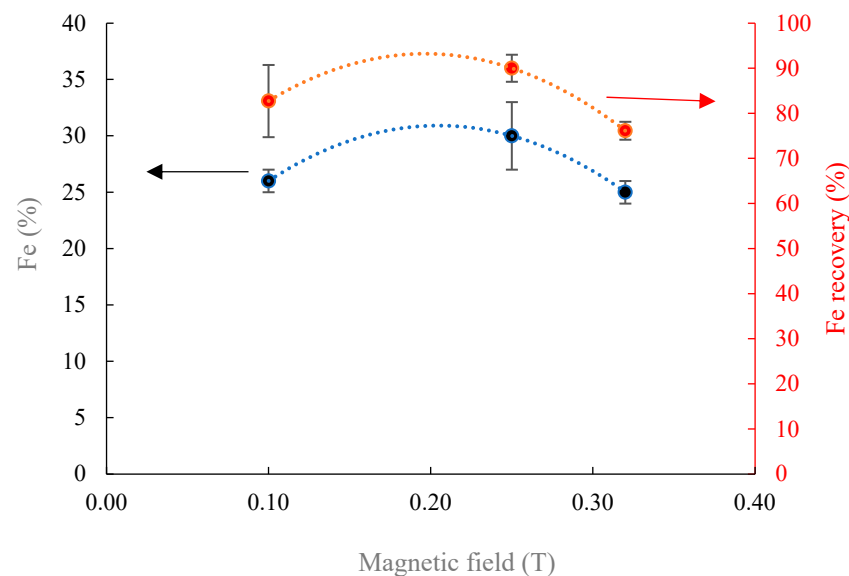


Figure 9. The effect of a magnetic field on the iron content and recovery for the feed size of $-212 + 106 \mu\text{m}$.

Figure 10 displays the grade-recovery curve for both particle ranges. As seen, finer particles show a lower recovery, but a substantially higher Fe grade compared to the coarser ones ($-212 + 106 \mu\text{m}$). On the other hand, coarser particles result in relatively excessive recoveries ($>76\%$) but grades lower than 30% which is not desirable and requires further beneficiation. Therefore, the optimum condition can be selected as the finer fraction size ($-106 + 74 \mu\text{m}$) where the Fe grade can be improved to ca. 32% with the recovery of 80%. Having this in mind, applying one-two stages of scavenging and/or cleaning may increase the Fe grade, which is highlighted as a future work and should be studied in detail.

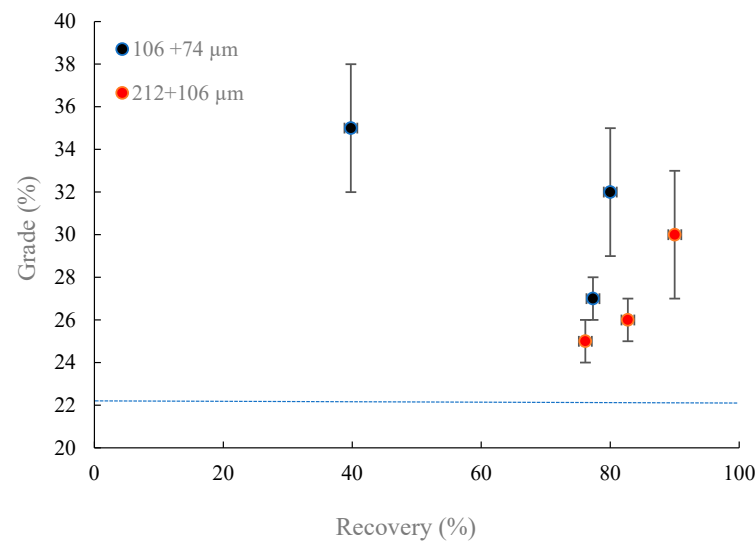


Figure 10. The iron grade-recovery curve for both particle size ranges (dash line represents the feed grade for both size fractions).

3.4.2. Wet Low-Intensity Magnetic Separation

Since the material contains elemental iron (Fe), which is a ferromagnetic type of material, a low magnetic field was applied, hoping to obtain a reasonable separation. Figure 11 illustrates the impact of using wet low-intensity magnetic separation (WLIMS) on the H₂-reduced bauxite residue at a fixed/permanent magnetic field of 0.035 T on two particle ranges. As seen, the iron content is enriched to 37% with a recovery of 55%. However, by reducing the size to $-212 + 106 \mu\text{m}$, there is only a 6% increase in the Fe content. It is worth noting that the coarser the particle, the more favorable the separation process is, but it leads to a lower liberation degree. Nevertheless, the non-magnetic part still contains a reasonable amount of iron, which is not desirable from process separation point of view. It can be concluded, based on the WLIMS data given in Figure 11, back-to-back processes are required, meaning high- (HIMS), medium- (MIMS) followed by low- (WLIMS) intensity magnetic separation.

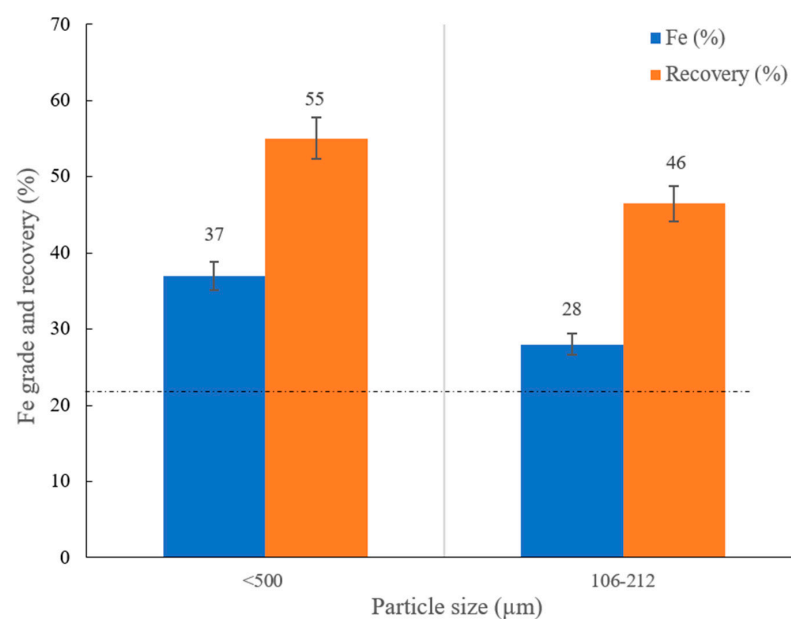


Figure 11. Effect of particle size on the separation of the studied sample using WLIMS (dash line represents the feed grade).

4. Conclusions and Future Works

This work aims at studying the reduction of a bauxite residue, calcite, and quick lime pellets using hydrogen, characterizing the product properties, and recovering iron using electrostatic and magnetic separation methods. The following are the main conclusions drawn from this investigation:

- The iron oxide present in the pellets is converted completely to metallic iron. The mass loss during the reduction of hydrogen, XRD, and SEM analysis indicates all Fe in metallic form in the reduced pellets. The alumina present in the bauxite residue is converted to the mayenite phase during hydrogen reduction and via reacting with adjacent calcium oxide.
- The size of metallic Fe particles in the reduced samples is 5–6 μm on average and they are mostly accumulated in the pellet with the oxide phases in between.
- During the physical separation of the reduced pellets, it is indicated that the electrostatic separation is not a suitable technique to separate iron from the rest of the materials due to an even distribution of Fe throughout the feed's matrix, fine iron particle sizes (5–6 μm), and the inefficiency of the process. Following the electrostatic experimental results on three different fraction sizes shows that there is only a slight improvement in Fe content, while most of the mass product transfers to the middling part.
- Magnetic separation outcomes using the Davis Tube under different magnetic fields on two different fraction sizes reveal that Fe magnitude could be improved from 22% to 35% at 0.1 T, which is reduced by increasing the magnetic intensity. Coarsening the particle size from $-106 + 74 \mu\text{m}$ to $-212 + 106 \mu\text{m}$ at the magnetic intensity of 0.1 T induces the attenuation of Fe grade from 35% to 25% and increases the iron recovery from 40% to 83%. Applying WLIMS on $-212 + 106 \mu\text{m}$ induces an increase on Fe content from 22% to 28% with the recovery of 46%.

According to the presented results given in this work the following items can be considered for future works:

- Since water-soluble components (e.g., Na-bearing phases) are present in the H_2 -reduced bauxite residue, water-leaching treatment before magnetic separation tests might be effective and need to be studied in detail.
- A continuous magnetic separation rather than a batch test for enhancing the Fe grade in final product can be considered for future test works.
- Two stages of roughing and cleaning back-to-back on the finer fraction sizes ($-106 + 74 \mu\text{m}$) can reach higher iron grade and recovery.
- The Mössbauer spectroscopy method is another promising technique for identifying valence state of iron (Fe^0 (metallic), Fe^{2+} and Fe^{3+}) in the studied sample.
- In addition to the XRF, XRD, and SEM-EDX analyses, the standard titrimetric analysis should be considered with the purpose of determining and correlating the content of metallic iron and total iron in the samples.

Author Contributions: Conceptualization, A.H. and M.K.K.; Methodology, A.H. and M.K.K.; Investigation, A.H. and M.K.K.; Validation, A.H., M.K.K., J.S. and P.B.K.; Data collection, A.H. and M.K.K.; Writing—original draft preparation, A.H. and M.K.K.; Review and editing, A.H., M.K.K., J.S. and P.B.K.; Visualization, A.H., M.K.K., J.S. and P.B.K.; Supervision, A.H., J.S. and P.B.K. All authors have read and agreed to the published version of the manuscript.

Funding: This study was performed and financially supported by The European Union's Horizon 2020 research and innovation program under the grant number of 958307 (HARARE project).

Data Availability Statement: Data will be available per request.

Acknowledgments: This study was performed and financially supported by The European Union’s Horizon 2020 research and innovation program under the grant number of 958307 (HARARE project). The authors are very thankful to Camilo Andrés Mena Silva, Kornel M. Tobiczkyk, Gustav Ward, and Henning Leonard Nygad Aune from the NTNU Mineral Processing Laboratory for their assistances regarding the physical separation tests works.

Conflicts of Interest: The authors declare that they have no known competing financial interests or personal relationships that could have appeared to influence the work reported in this paper.

Appendix A

Primary results of CarpcO electrostatic tests on coarse fraction sizes (>1397 μm , –1397 + 500 μm and <500 μm) where the outcomes of only <500 μm fraction size are presented in Table A1.

Table A1. Results of electrostatic tests on <500 μm size fraction (Feed = 100 g and Fe content in feed = 20%).

	Products		
	Non-Conductive	Middling	Conductive
Fe (%)	23	22	20
Recovery (%)	65	32	5

References

- Balat, M. Potential importance of hydrogen as a future solution to environmental and transportation problems. *Int. J. Hydrogen Energy* **2008**, *33*, 4013–4029. [CrossRef]
- Ritchie, H.; Roser, M.; Rosado, P. CO₂ and Greenhouse Gas Emissions. Our World Data. 2020. Available online: <https://ourworldindata.org/co2-and-greenhouse-gas-emissions> (accessed on 3 April 2023).
- Wang, P.; Ryberg, M.; Yang, Y.; Feng, K.; Kara, S.; Hauschild, M.; Chen, W.Q. Efficiency stagnation in global steel production urges joint supply- and demand-side mitigation efforts. *Nat. Commun.* **2021**, *12*, 2066. [CrossRef] [PubMed]
- Trollip, H.; McCall, B.; Bataille, C. How green primary iron production in South Africa could help global decarbonization. *Clim. Policy* **2022**, *22*, 236–247. [CrossRef]
- Association, W.S. *Climate Change and the Production of Iron and Steel Transforming Steel Production*; World Steel Association: Brussels, Belgium, 2021.
- Pineau, A.; Kanari, N.; Gaballah, I. Kinetics of reduction of iron oxides by H₂: Part I: Low temperature reduction of hematite. *Thermochim. Acta* **2006**, *447*, 89–100. [CrossRef]
- Skibelid, O.B.; Velle, S.O.; Volla, F.; Van der Eijk, C.; Hoseinpour-Kermani, A.; Safarian, J. Isothermal hydrogen reduction of a lime-added bauxite residue agglomerate at elevated temperatures for iron and alumina recovery. *Materials* **2022**, *15*, 6012. [CrossRef]
- Pilla, G.; Kapelari, S.V.; Hertel, T.; Blanpain, B.; Pontikes, Y. Hydrogen reduction of bauxite residue and selective metal recovery. *Mater. Today Proc.* **2022**, *57*, 705–710. [CrossRef]
- Hassanzadeh, A.; Pilla, G.; Hertel, T.; Pontikes, Y.; Kowalczyk, P.B. H₂-reduction of bauxite residue and iron recovery through magnetic separation. In Proceedings of the 17th International Mineral Processing Symposium, Istanbul, Türkiye, 15–17 December 2022; pp. 223–243.
- Lazou, A.; van der Eijk, C.; Balomenos, E.; Kolbeinsen, L.; Safarian, J. On the direct reduction phenomena of bauxite ore using H₂ gas in a fixed bed reactor. *J. Sustain. Metall.* **2020**, *6*, 227–238. [CrossRef]
- Bahmani-Ghaedi, A.; Hassanzadeh, A.; Sam, A.; Entezari-Zarandi, A. The effect of residual flocculants in the circulating water on dewatering of Gol-e-Gohar iron ore. *Miner. Eng.* **2022**, *179*, 107440. [CrossRef]
- Kossoff, D.; Dubbin, W.E.; Alfredsson, M.; Edwards, S.J.; Mackline, M.G.; Hudson-Edwards, K.A. Mine tailings dams: Characteristics, failure, environmental impacts, and remediation. *Appl. Geochem.* **2014**, *51*, 229–245. [CrossRef]
- Mayes, W.M.; Burke, I.T.; Gomes, H.I.; Anton, A.D.; Molnar, M.; Feigl, V.; Ujaczki, E. Advances in understanding environmental risks of red mud after the Ajka spill, Hungary. *J. Sustain. Metall.* **2016**, *2*, 332–343. [CrossRef]
- Do Carmo, F.F.; Kamino, L.H.Y.; Junior, R.T.; Campos, I.C.; Do Carmo, F.F.; Silvino, G.; Castro, K.J.S.X.; Mauro, M.L.; Rodrigues, N.U.A.; Mirand, M.P.S.; et al. Fundão tailings dam failures: The environment tragedy of the largest technological disaster of Brazilian mining in global context. *Perspect. Ecol. Conserv.* **2017**, *15*, 145–151. [CrossRef]
- Adamson, A.N.; Bloore, E.J.; Carr, A.R. Basic Principles of Bayer Process Design. In *Extractive Metallurgy of Aluminum*; Springer: Cham, Switzerland; New York, NY, USA, 1962; Volume 1, pp. 23–57. ISBN 978-3-319-48574-4. [CrossRef]
- Klauber, B.C.; Gräfe, M.; Power, G. Bauxite residue issues: II. options for residue utilization. *Hydrometallurgy* **2011**, *108*, 11–32. [CrossRef]

17. Liu, Y.; Naidu, R. Hidden values in bauxite residue (red mud): Recovery of metals. *Waste Manag.* **2014**, *34*, 2662–2673. [[CrossRef](#)]
18. Guo, Y.H.; Gao, J.J.; Xu, H.J.; Zhao, K.; Shi, X.F. Nuggets production by direct reduction of high iron red mud. *J. Iron Steel Res. Int.* **2013**, *20*, 24–27. [[CrossRef](#)]
19. Uzun, D.; Gulfen, M. Dissolution kinetics of iron and aluminium from red mud in sulphuric acid solution. *Indian J. Chem. Technol.* **2007**, *14*, 263–268.
20. Safarian, J. Extraction of iron and ferrosilicon alloys from low-grade bauxite ores. In *The Minerals, Metals & Materials Series*; Springer: Cham, Switzerland, 2018. [[CrossRef](#)]
21. Cengeloglu, Y.; Kir, E.; Ersoz, M.; Buyukerkek, T.; Gezgin, S. Recovery and concentration of metals from red mud by Donnan dialysis. *Colloids Surf. A Physicochem. Eng. Asp.* **2003**, *223*, 95–101. [[CrossRef](#)]
22. Jamieson, E.; Jones, A.; Cooling, D.; Stockton, N. Magnetic separation of Red Sand to produce value. *Miner. Eng.* **2006**, *19*, 1603–1605. [[CrossRef](#)]
23. Sadangi, J.K.; Das, S.P.; Tripathy, A.; Biswal, S.K. Investigation into recovery of iron values from red mud dumps. *Sep. Sci. Technol.* **2018**, *53*, 2186–2191. [[CrossRef](#)]
24. Habibi, H.; Pirouzan, D.; Shakibania, S.; Pourkarimi, Z.; Mokmeli, M. Physical and chemical separation of Ti, rare earth elements, Fe, and Al from red mud by carbothermal reduction, magnetic separation, and leaching. *Environ. Sci. Pollut. Res.* **2022**, *29*, 62952–62972. [[CrossRef](#)]
25. Gotsu, S.; Mishra, B.; Martins, G. Extraction of iron from red mud: Low temperature reduction to magnetite and magnetic separation. In Proceedings of the 2nd International Bauxite Residue Valorization and Best Practices Conference, Athens, Greece, 10 May 2018; pp. 7–10.
26. Ksiazek, M.; Ringdalen, E.; Hogaas, P.H.; van der Eijk, C. Iron removal from bauxite ores. In Proceedings of the 2nd International Bauxite Residue Valorization and Best Practices Conference, Athens, Greece, 10 May 2018; pp. 39–52.
27. Samuila, A.; Iuga, A.; Morar, R.; Neamatu, V.; Dascalescu, L. Electrostatic technologies for materials recovery in high-intensity electric fields. *Mater. Sci.* **2007**, *1*, 629–687.
28. Gupta, A.; Yan, D. *Mineral Processing Design and Operations*, 2nd ed.; Elsevier: Amsterdam, The Netherlands, 2016; ISBN 978-0-444-63589-1. [[CrossRef](#)]
29. Chelgani, S.C.; Asimi Neisiani, A. Electrostatic Separation. In *Dry Mineral Processing*; Springer: Cham, Switzerland, 2022. [[CrossRef](#)]
30. Kar, M.K.; van der Eijk, C.; Safarian, J. Hydrogen reduction of high temperature sintered and self-hardened pellets of bauxite residue produced via the addition of limestone and quicklime, TRAVAUX 51. In Proceedings of the 40th International ICSOBA Conference, Athens, Greece, 10–14 October 2022; pp. 823–833.
31. Monsen, B.E.; Thomassen, E.S.; Bragstad, I.; Ringdalen, E.; Hoegaas, P.H. Characterization of DR pellets for DRI applications. In Proceedings of the AISTech Conference, Cleveland, OH, USA, 3–7 May 2015; Volume 1, pp. 1–11.
32. Wills, B.A.; Finch, J.A. *Wills' Mineral Processing Technology: An Introduction to the Practical Aspects of Ore Treatment and Mineral Recovery*, 8th ed.; Butterworth-Heinemann: Oxford, UK, 2015; pp. 381–407. [[CrossRef](#)]
33. Dance, A.D.; Morrison, R.D. Quantifying a black art: The electrostatic separation of mineral sands. *Miner Eng.* **1992**, *5*, 751–765. [[CrossRef](#)]
34. Dötterl, M.; Wachsmuth, U.; Waldmann, L.; Flachberger, H.; Mirkowska, M.; Brands, L.; Beier, P.M.; Stahl, I. *Electrostatic Separation, Ullmann's Encyclopedia of Industrial Chemistry*; Wiley-VCH Verlag GmbH & Co. KGaA: Weinheim, Germany, 2016; pp. 1–35. [[CrossRef](#)]
35. Pilla, G.; Hertel, T.; Blanpain, B.; Pontikes, Y. Influence of H₂ content on Fe, Al and Na Recovery during low-temperature reduction of bauxite residue. In Proceedings of the 8th International Slag Valorisation Symposium, Mechelen, Belgium, 16 November 2023; pp. 146–149.
36. Kapelari, S.; Gamaletsos, P.N.; Pilla, G.; Pontikes, Y.; Blanpain, B. Developing a Low-Temperature, Carbon-Lean Hybrid Valorisation Process for Bauxite Residue (Red Mud) Towards Metallic Fe and Al Recovery. *J. Sustain. Metall.* **2023**, *9*, 1–10. [[CrossRef](#)]

Disclaimer/Publisher's Note: The statements, opinions and data contained in all publications are solely those of the individual author(s) and contributor(s) and not of MDPI and/or the editor(s). MDPI and/or the editor(s) disclaim responsibility for any injury to people or property resulting from any ideas, methods, instructions or products referred to in the content.